Doublon bound states in the continuum through giant atoms

Walter Rieck [1,2] Anton Frisk Kockum [1,*] and Guangze Chen [1,†]
[1]*Department of Microtechnology and Nanoscience, Chalmers University of Technology, 41296 Gothenburg, Sweden*
[2]*Department of Physics, Stockholm University, 10691 Stockholm, Sweden*

(Received 30 November 2025; accepted 21 October 2026; published 17 November 2026)

Bound states in the continuum (BICs) are spatially localized modes embedded in the spectrum of extended states, typically stabilized by symmetry or interference. While extensively studied in single-particle and linear systems, the many-body regime of BICs remains largely unexplored. Here, we show that giant atoms, quantum emitters coupled nonlocally to structured waveguides, can host robust doublon BICs, i.e., two-photon bound states stabilized by destructive interference and interactions. We first analyze a driven two-photon emission process and show how doublon BICs arise and mediate decoherence-free interaction between distant atoms. We then show that these doublon BICs also emerge under natural, undriven dynamics via a virtual two-photon emission process in three-level giant atoms. Our results put forward giant atoms as a platform to realize two- and eventually many-body BICs, revealing an interference-based mechanism for stabilizing many-body localized states.

DOI: 10.1103/1zkl-j8tk

I. INTRODUCTION

Bound states in the continuum (BICs) are spatially localized eigenstates that exist within the continuous spectrum of extended, radiative modes [1,2]. They can arise through mechanisms such as symmetry protection [3], separability of variables [4], or destructive interference between leakage channels [5–7]. BICs have been extensively studied in photonic and acoustic systems [8–13], where their unique combination of spatial confinement and spectral embedding gives rise to exceptionally long lifetimes and sharp resonances. Crucially, their in-band nature enables efficient coupling to external radiation or nearby modes, while their bounded character ensures strong field localization. These properties make BICs ideal platforms for many applications, including nonlinear optical enhancement [14–19], coherent light generation [20–23], and ultrasensitive sensing [24–28].

Recently, there has been growing interest in extending the concept of BICs to the many-body regime, where they could offer new mechanisms for suppressing thermalization [29]. However, this regime remains largely unexplored. Existing studies typically rely on impurity-induced localization [29–31], which requires engineered on-site potentials and is therefore experimentally challenging, or on boundary effects [32], where the resulting BICs are tied to the system's boundary and offer limited flexibility for applications. This motivates the search for new platforms and mechanisms to realize many-body BICs in a more controllable manner.

Giant atoms (GAs)—quantum emitters coupled to a waveguide at multiple, spatially separated points—have emerged in the past decade as a versatile platform for exploring nonlocal and interference-driven light-matter interactions [33]. As shown both theoretically [34–57] and experimentally for several systems [58–71], the nonlocal coupling of GAs results in interference effects that alter spontaneous emission and give rise to phenomena beyond conventional quantum optics. A striking example is the emergence of decoherence-free interaction (DFI) [36,63], where multiple GAs interact coherently through a waveguide without radiative losses into the waveguide. Notably, the DFI can be understood as a manifestation of BICs [38,48,51,72], which arise due to destructive interference between emission pathways that cancels radiation into the waveguide. Despite the connection between GAs and BICs, studies of BICs in giant-atom systems have so far been restricted to the single-excitation regime.

In this article, we propose a mechanism to realize many-body BICs through destructive interference in giant-atom systems, focusing on the emergence of doublon BICs—two-photon bound states that remain localized despite lying within the radiation continuum of a structured waveguide. We begin by analyzing a driven two-photon emission process for a single two-level GA, demonstrating how these states arise from the interplay between interactions and interference, which suppresses decay into the waveguide. We then show that doublon BICs can mediate DFI between two GAs, reinforcing their physical significance. Going beyond this illustrative setup, we show that doublon BICs and their associated DFI can also emerge under undriven dynamics with realistic coupling configurations for three-level GAs. We finally discuss how our proposal can be realized on several experimental

*Contact author: anton.frisk.kockum@chalmers.se
†Contact author: guangze@chalmers.se

Published by the American Physical Society under the terms of the Creative Commons Attribution 4.0 International license. Further distribution of this work must maintain attribution to the author(s) and the published article's title, journal citation, and DOI. Funded by Bibsam.

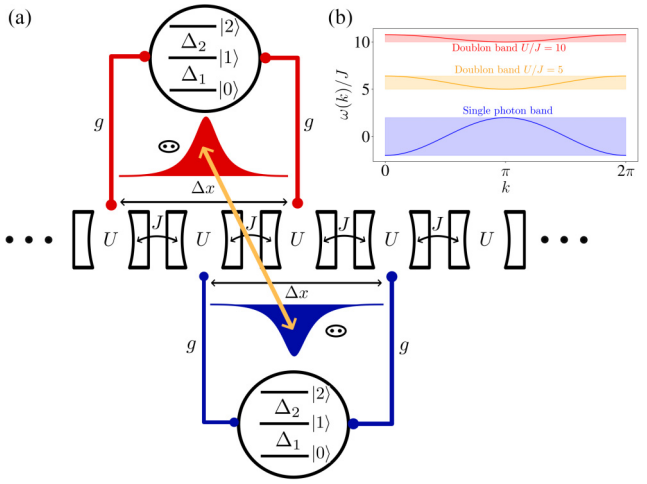


FIG. 1. Overview of the system. (a) Schematic of two three-level GAs coupled to a structured waveguide with nearest-neighbor hopping rate J and on-site two-photon interaction U. Each atom has level spacings detuned by $\Delta_{1,2}$ from the band center and is coupled to the waveguide at two points, spatially separated with distance $\Delta x = 2$, forming a braided configuration. The coupling strength at each connection point is g. For appropriate level spacings, doublon BICs emerge via interference between emission pathways. The overlap of these doublon BICs between the two atoms mediates a decoherence-free interaction (orange arrow). (b) Band structure of the nonlinear waveguide, for two different values of U.

platforms and its potential applications in generating and distributing many-body entangled states.

II. MODEL

We consider a system of multiple GAs coupled to a structured waveguide [see Fig. 1(a)]. The total Hamiltonian for this system is

$$H = H_A + H_B + H_{\rm int}, \tag{1}$$

where H_A and H_B are the bare Hamiltonians for the atoms and the bath (waveguide), respectively, and $H_{\rm int}$ describes their interaction.

The bath we consider is a one-dimensional array of N coupled cavities with nearest-neighbor hopping J and on-site Kerr nonlinearity U. Without loss of generality, we work in a frame rotating at ω_c, the center of the bath band. The bare bath Hamiltonian in this rotating frame is thus

$$H_B = \sum_{n=1}^{N} \frac{U}{2} a_n^\dagger a_n^\dagger a_n a_n - \sum_{n=1}^{N-1} J\left(a_n^\dagger a_{n+1} + \text{H.c.}\right), \tag{2}$$

where a_n ($a_n^\dagger$) is the photon annihilation (creation) operator for cavity n and H.c. denotes Hermitian conjugate.

The Kerr nonlinearity U supports the formation of doublons—two-photon bound states where the photons tend to stay near each other [30,73–76]. A doublon with momentum k has the wavefunction [74,75]

$$|\psi_D(k)\rangle = \frac{1}{\sqrt{2}} \sum_{m=1}^{N} \sum_{n=1}^{N} e^{ik\frac{(m+n)}{2}} e^{-\frac{|m-n|}{\varsigma(k)}} a_m^\dagger a_n^\dagger |\text{vac}\rangle, \tag{3}$$

where $\varsigma(k)$ is the momentum-dependent localization length and $|\text{vac}\rangle$ is the vacuum state. These doublons can propagate through the waveguide and have the dispersion relation [74,75]

$$\omega_D(k) = \text{sgn}(U)\sqrt{U^2 + 16J^2 \cos^2\left(\frac{k}{2}\right)}. \tag{4}$$

Notably, when $U > 4J$, the doublon band becomes energetically separated from the continuum of two unbound photons [see Fig. 1(b)]. This separation allows us to isolate doublon-mediated dynamics by tuning the atomic level spacings to match the doublon dispersion.

Since our study involves multiphoton processes, we model each GA as a three-level system. For simplicity, we assume that all atoms have an identical ladder-type level structure, with ω_1 (ω_2) the level spacing between the $|0\rangle$ ($|1\rangle$) and $|1\rangle$ ($|2\rangle$) levels of the atom. The bare Hamiltonian for N_a GAs is then, in the frame rotating at ω_c,

$$H_A = \sum_{n=1}^{N_a} \left[(\Delta_2 + \Delta_1) \frac{\sigma_n^{(2),+}\sigma_n^{(2),-}}{2} + \Delta_1 \sigma_n^{(1),+}\sigma_n^{(1),-} \right], \tag{5}$$

where $\Delta_j = \omega_j - \omega_c$ and the ladder operators act as

$$\sigma_n^{(j),+}|j-1\rangle = \sqrt{j}|j\rangle, \qquad \sigma_n^{(j),-}|j\rangle = \sqrt{j}|j-1\rangle. \tag{6}$$

III. DIRECT TWO-PHOTON EMISSION

The key ingredient of GAs is the multiple-point coupling: Each GA n is coupled to the waveguide at p_n different cavities with strength g. To illustrate how this multipoint coupling can result in a doublon BIC, we first consider a direct two-photon emission process described by the interaction Hamiltonian

$$H_{\rm int} = g \sum_{n=1}^{N_a} \sum_{j=1}^{p_n} \left[\sigma_n^{(1),+} a_{x_{nj}} a_{x_{nj}} + \text{H.c.}\right], \tag{7}$$

where x_{nj} is the jth coupling point of atom n. Although we here mostly use this type of nonlinear coupling for illustrative purposes, it can be engineered experimentally using external drives [77] or a superconducting quantum interference device [78]. If the two-photon operator in Eq. (7) is replaced with a single-photon operator, it is known that single-photon BICs can emerge due to destructive interference between multiple coupling points [34]. In our case, since two photons are created (or annihilated) at the same site, the resulting state has significant overlap with doublon modes. Thus, we expect a doublon BIC if the atomic level spacing Δ_1 lies within the doublon band.

To demonstrate this explicitly, we numerically simulate a system of $N = 199$ cavities, where a single GA couples to sites $x_{11} = 99$ and $x_{12} = 101$, i.e., a separation $\Delta x = 2$. A doublon BIC arises due to destructive interference between emission paths [34], governed by the decoherence-free (DF) condition $1 + \exp(ik\Delta x) = 0$, which is satisfied with

$$k_{\rm DF} = \frac{(2n+1)\pi}{\Delta x}, \quad n \in \mathbb{N}. \tag{8}$$

For $\Delta x = 2$, this yields $k_{\rm DF} = \pm\pi/2$; the corresponding doublon frequency is $\omega_{\rm DF} = \omega_D(k_{\rm DF})$. Thus, setting $\Delta_1 = \omega_{\rm DF}$

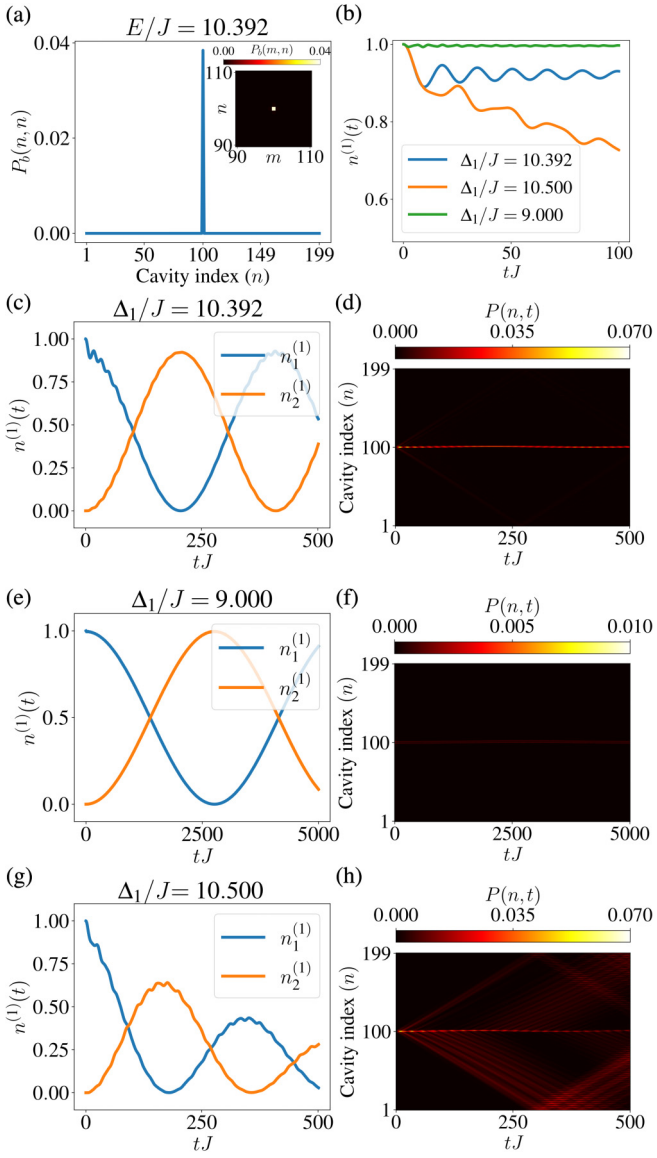


FIG. 2. Doublon BIC and DFI between GAs, for two-photon interaction [Eq. (7)]. Parameters: $U = 10J$, $g = 0.04J$, and $\Delta x = 2$. (a) The doublon BIC for a single GA with the DF frequency $\Delta_1 = 10.392J$. The plot shows the bound state's overlap $P_b(n, n)$ with the two-photon states $|0, nn\rangle$, while the inset also shows the off-diagonal elements $P_b(m, n)$. (b) Time evolution of the population $n^{(1)}(t)$ of the GA's $|1\rangle$ level for three values of Δ_1: at the DF frequency (blue), inside the doublon band (orange), and outside the doublon band (green). (c) Population dynamics $n^{(1)}_{1,2}(t)$ of two braided GAs at the DF frequency. (d) Heatmap of the doublon population $P(n, t) = \langle\psi(t)|a_n^\dagger a_n^\dagger a_n a_n|\psi(t)\rangle$ in the waveguide. (e), (f) Same as in panels (c) and (d) but for a frequency outside the doublon band. (g), (h) Same as in panels (c) and (d), but for a non-DF frequency inside the doublon band.

enables the formation of a doublon BIC, which is shown in Fig. 2(a) for $U = 10J$ and $g = 0.04J$ (chosen to remain in the Markovian regime).

We identify the BIC state $|\psi_b\rangle$ using the inverse participation ratio [79,80]. Its overlap with the two-photon basis state $|0, mn\rangle = a_m^\dagger a_n^\dagger|\text{vac}\rangle$, denoted as $P_b(m, n) = |\langle 0, mn|\psi_b\rangle|$, confirms that it is a doublon BIC: The overlap becomes exponentially small when $m \neq n$ [inset of Fig. 2(a)], a typical characteristic of a doublon; additionally, the wavefunction is localized in space, demonstrating its bound nature.

In Fig. 2(b), we plot the atom's $|1\rangle$-level population $n^{(1)}(t) = \langle\psi(t)|\sigma^{(1),+}\sigma^{(1),-}|\psi(t)\rangle$ for three different atomic frequencies, starting from $|\psi(t = 0)\rangle = \sigma^{(1),+}|\text{vac}\rangle$. When $\Delta_1 = \omega_{\text{DF}}$ (blue curve), this population stabilizes at a high value, typical of a BIC. In contrast, for Δ_1 within the doublon band (orange curve), the atom population displays exponential decay due to coupling to radiative modes instead of the doublon BIC. For Δ_1 outside the doublon band (green curve), the atomic population shows decoherence-free behavior due to the formation of a bound state outside the continuum (BOC) [81].

A key distinction between BICs and conventional BOCs is that BICs reside within the band, enabling significantly faster DFI between multiple GAs. To illustrate this, we add a second GA coupled to cavities 100 and 102, forming the braided configuration shown in Fig. 1(a). This configuration is known to be essential for enabling overlap between BICs associated with different atoms, a prerequisite for DFI [36,51]. As shown in Fig. 2(c), starting from $|\psi(t = 0)\rangle = \sigma_1^{(1),+}|\text{vac}\rangle$, this setup leads to coherent oscillations between the two atoms, except for a leakage at early times due to non-Markovian effects [49]. Owing to energy conservation, this leakage can only populate doublon states that are not spatially localized. The leakage can be suppressed by reducing g [82]. The corresponding doublon population in the waveguide $P(n, t) = \langle\psi(t)|a_n^\dagger a_n^\dagger a_n a_n|\psi(t)\rangle$ is shown in Fig. 2(d), revealing no doublon leakage during the DFI. In contrast, when the atoms' frequencies are tuned outside the doublon band, BOCs form instead of BICs, resulting in a DFI with much slower rate [Figs. 2(e) and 2(f)].

We note that a detuning from ω_{DF} not only suppresses the formation of BIC, but also allows partial population of the extended doublon modes. As a consequence, the DFI is disrupted [Fig. 2(e)] and doublon leakage into the waveguide becomes prominent [Fig. 2(f)].

IV. SINGLE-PHOTON COUPLING

Above, we showed the emergence of doublon BICs and the associated DFI between GAs coupled to a structured waveguide, using the direct two-photon coupling in Eq. (7). While that example is illustrative and conceptually clear, the two-photon coupling that it relies on generally requires external drives. We now turn to a more practical, and theoretically more intriguing, scenario based on common single-photon coupling with three-level GAs:

$$H_{\text{int}} = g\sum_{n=1}^{N_a}\sum_{j=1}^{p_n}\left[\sigma_n^{(1),+}a_{x_{nj}} + \sigma_n^{(2),+}a_{x_{nj}} + \text{H.c.}\right]. \quad (9)$$

Here, two-photon emission only becomes possible (through successive single-photon emission) when an atom is initialized in its $|2\rangle$ state, making the emergence of doublon BICs less intuitive and more conceptually rich. Note that the $|1\rangle \leftrightarrow |2\rangle$ transition couples $\sqrt{2}$ more strongly to the structured waveguide than the $|0\rangle \leftrightarrow |1\rangle$ transition. This factor $\sqrt{2}$ is

implicitly included in Eq. (9) through the definition of $\sigma_n^{(1),+}$ in Eq. (6).

To form a doublon BIC under the interaction in Eq. (9), the energy of the $|2\rangle$ level must match the doublon dispersion, i.e., $\Delta_1 + \Delta_2 \sim U$ [see Fig. 1(b)]. Additionally, to suppress single-photon emission into the waveguide, both transition energies must lie outside the single-photon band: $|\Delta_{1,2}| > 2J$. In this regime, the $|2\rangle$ state of the atom couples to doublon modes via a second-order process with an effective coupling strength $g_{\text{eff}} \sim g^2/\Delta_2$ [80] to the doublon modes in the waveguide. This effective coupling is essential to the formation of doublon BICs in this setup. An additional effect of the second-order process is that it adds a Lamb shift to the energy of the $|2\rangle$ state and a correction to the doublon dispersion [80].

Due to the second-order coupling process, a doublon BIC can form at decoherence-free frequencies. Notably, the decoherence-free frequency has been modified to $\omega_{\text{DF}} = \Delta_1 + \Delta_2 + \Delta$, as numerically demonstrated with parameters $g = 0.25J$, $\Delta_1 = 5.338J$, $\Delta_2 = 5J$, and $\Delta = 0.054J$ [Fig. 3(a)]. The additional Δ is due to the Lamb shift in the atomic levels [80]. To confirm the BIC, we examine, in Fig. 3(b), the $|2\rangle$-level occupation $n^{(2)}(t) = \langle\psi(t)|\sigma^{(2),+}\sigma^{(2),-}|\psi(t)\rangle/2$ for different atomic frequencies,, starting from $|\psi(t=0)\rangle = \sigma^{(2),+}\sigma^{(1),+}|\text{vac}\rangle/\sqrt{2}$. At $\Delta_1 + \Delta_2 + \Delta = \omega_{\text{DF}}$ (blue curve), we observe a decoherence-free behavior where the population stabilizes at a high value. The dynamics for $\Delta_1 + \Delta_2 + \Delta \neq \omega_{\text{DF}}$ inside (orange curve) and outside (green curve) the band are similar to those in Fig. 2(b), and distinct from the BIC behavior.

We show the occurrence of DFI under this single-photon coupling in Figs. 3(c) and 3(d), where, as in Figs. 2(c) and 2(d), we add a second GA coupled to cavities 100 and 102, forming a braided configuration. Starting from $|\psi(t=0)\rangle = \sigma_1^{(2),+}\sigma_1^{(1),+}|\text{vac}\rangle/\sqrt{2}$, we observe coherent doublon-mediated dynamics between two GAs in the same way as in the preceding section. We see that due to the weaker effective coupling, the exchange rate between the GAs is slower than that in Fig. 2(c) (even though g is larger in Fig 3 than in Fig 2). Consequently, the doublon population being exchanged in Fig. 3(d) is smaller than that in Fig. 2(d). Aside from these quantitative differences, the DFI behavior remains qualitatively the same as in the two-photon coupling case. When the atoms' frequencies are tuned outside the doublon band, the rate of the DFI is much slower [Figs. 3(e) and 3(f)]. A small detuning from the decoherence-free condition leads to the breakdown of DFI and leakage of doublons, as shown in Figs. 3(g) and 3(h), further confirming the role of doublon BICs in mediating the DFI.

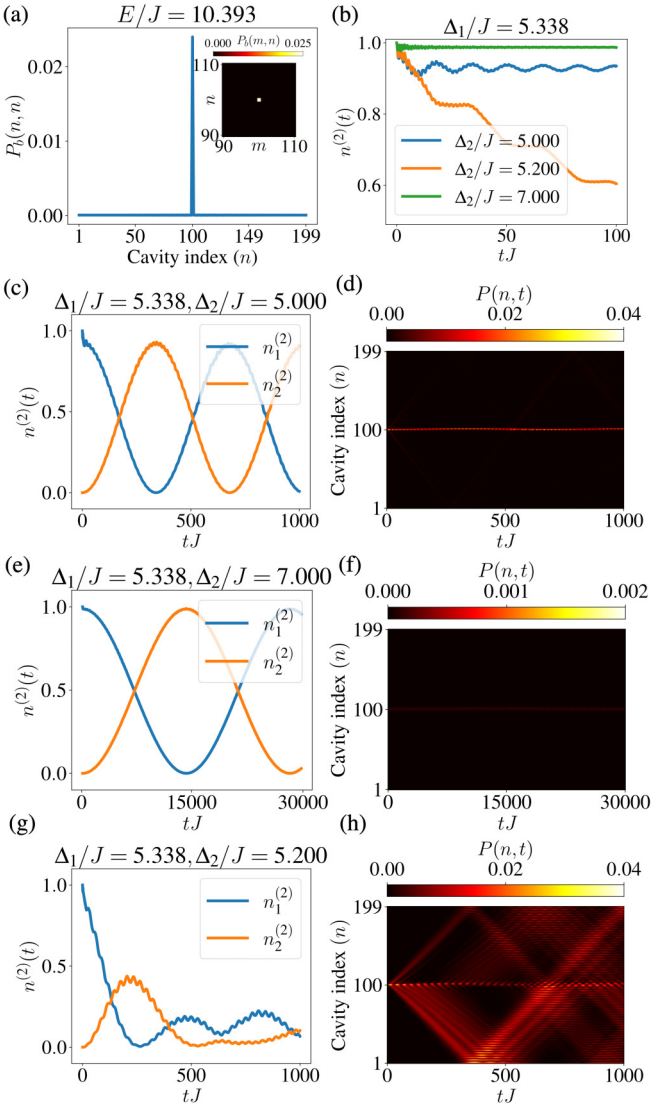


FIG. 3. Doublon BIC and DFI between GAs, for single-photon coupling [Eq. (9)]. Parameters: $U = 10J$, $g = 0.25J$, and $\Delta x = 2$. (a) The doublon BIC for a single GA with the DF condition $\Delta_1 = 5.338J$ and $\Delta_2 = 5J$. The plot shows the diagonal overlap $P_b(n,n)$, indicating strong localization in real space. The inset shows the full two-photon amplitude $P_b(m,n)$, with vanishing off-diagonal elements confirming the doublon nature. (b) Time evolution of the population $n^{(2)}(t)$ of the GA's $|2\rangle$ level for fixed $\Delta_1 = 5.338J$ and varying Δ_2: at the DF condition (blue), inside the doublon band (orange), and outside the doublon band (green). (c) Population dynamics $n_{1,2}^{(1)}(t)$ of two braided GAs at the DF frequency. (d) Heatmap of the doublon population $P(n,t) = \langle\psi(t)|a_n^\dagger a_n^\dagger a_n a_n|\psi(t)\rangle$ in the waveguide. (e), (f) Same as in panels (c) and (d), but for a frequency outside the doublon band. (g), (h) Same as in panels (c) and (d), but for a non-DF frequency inside the doublon band.

V. EXPERIMENTAL FEASIBILITY

To discuss the feasibility of experimentally demonstrating the effects presented in the preceding sections, we focus on a realization of our setup using superconducting transmon qubits [83] as the atoms, and coupled microwave resonators as the waveguide. Such setups have already been used to realize giant atoms [71].

To enable strong DFI between the atoms, a large J is preferred. The intercavity coupling between microwave resonators can reach at least $J/2\pi \approx 200\,\text{MHz}$ [84]. The corresponding Kerr nonlinearity $U = 10J \approx (2\pi) \times 2\,\text{GHz}$ used in the numerical simulations in Fig. 3 can be achieved with state-of-the-art resonators [85–87], and a qubit-resonator coupling of $g = J/4 = (2\pi) \times 50\,\text{MHz}$ is standard [88]. With these parameters, the DFI oscillation period in Fig. 3(c) is $t \approx 0.5\,\mu\text{s}$—this is much smaller than state-of-the-art

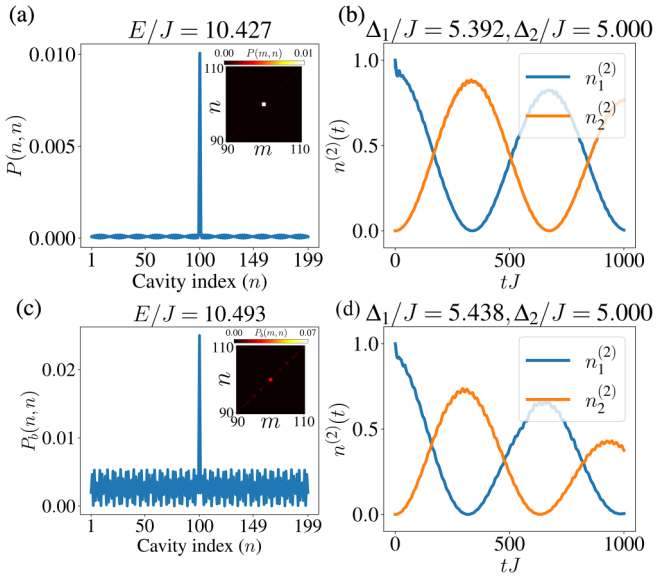


FIG. 4. Sensitivity of doublon BICs and DFI dynamics to emitter-frequency detuning for $U = 10J$, $g = 0.25J$, $\Delta x = 2$, and $\Delta_2 = 5J$. (a), (b) Doublon BIC and corresponding DFI dynamics for $\Delta_1 = 5.392J$, which has a detuning of $0.054J$ from the decoherence-free point in Fig. 3(a). (c), (d) Doublon BIC and corresponding DFI dynamics for $\Delta_1 = 5.438J$, which has a detuning of 0.1 from the decoherence-free point in Fig. 3(a).

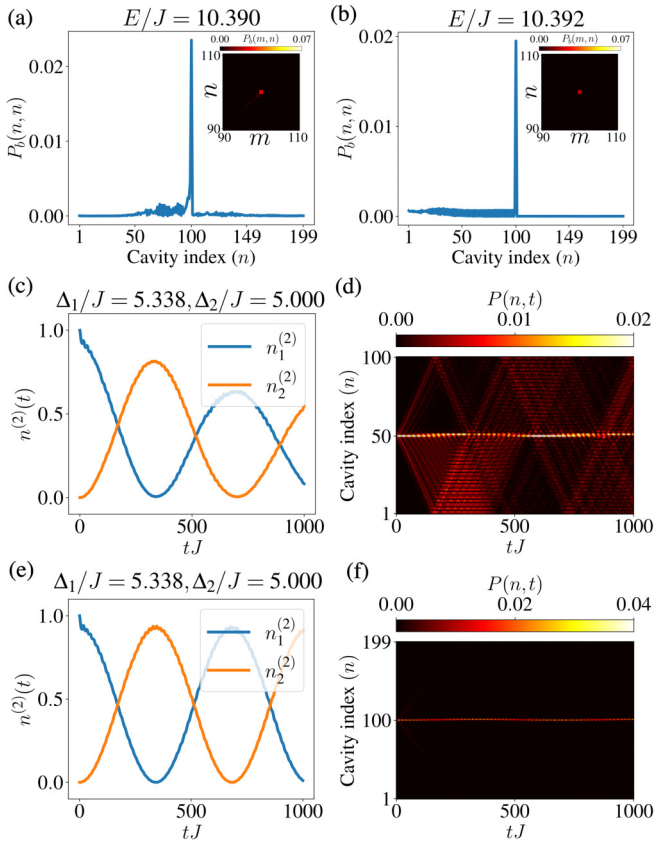


FIG. 5. Effect of resonator-frequency disorder on doublon BICs and DFI dynamics. (a), (b) Doublon BICs for disorder strengths $\delta\omega = 0.05J$ and $0.01J$, respectively. (c), (d) DFI dynamics for $\delta\omega = 0.05J$. (e), (f) DFI dynamics for $\delta\omega = 0.01J$. Other parameters are the same as in Fig. 3(a).

transmon-qubit lifetimes, which are tens or hundreds of microseconds [89–97].

In experiments, several imperfections can arise in addition to decoherence. Such imperfections include variations of the qubits' and resonators' frequencies, and of the coupling rates between the resonators. Below, we analyze these three potential imperfections and their effects one by one.

Since the BIC mechanism relies on interference and the doublon band is relatively narrow, the decoherence-free condition is sensitive to emitter-frequency variations. For the parameters $U = 10J$ considered here, the doublon bandwidth is approximately J. As shown in Figs. 4(a) and 4(b), a detuning of $0.054J$ from the decoherence-free point only weakly perturbs the BIC and DFI dynamics. However, a larger deviation of $0.1J$ [Figs. 4(c) and 4(d)] produces substantial leakage into extended states and noticeably reduces the DFI fidelity. For $J/2\pi \approx 200$ MHz, this corresponds to a tolerable frequency variation of approximately 10 MHz, which lies within the range of postfabrication tuning possible for current fixed-frequency transmon-qubit platforms, which is at least between 50 and 100 MHz [98] and likely much more [99], while fabrication imprecision is tens of megahertz [100].

To analyze resonator-frequency disorder, we randomly vary the cavity frequencies within an interval $[-\delta\omega, \delta\omega]$. The results from these numerical simulations are shown in Fig 5. We find that moderate disorder ($\delta\omega = 0.01J$) preserves both the spatial localization of the BIC [Fig. 5(b)] and the associated decoherence-free interaction dynamics [Figs. 5(e) and 5(f)], while stronger disorder ($\delta\omega = 0.05J$) leads to significant leakage of the BIC into extended doublon states [Fig. 5(a)] and worsens the DFI [Figs. 5(c) and 5(d)]. For experimentally relevant parameters $J/2\pi \approx 200$ MHz [84], this corresponds to a tolerable disorder scale below approximately $\delta\omega/2\pi < 2$ MHz, which is within the range demonstrated in superconducting-resonator arrays [101,102].

We also considered disorder in the intercavity couplings by sampling couplings uniformly from an interval $[J - \delta J, J + \delta J]$. The results from these numerical simulations are shown in Fig. 6. As illustrated in Figs. 6(a) and 6(b), the doublon BICs remain robust even for $\delta J = 0.1J$ and $\delta J = 0.2J$. As a consequence, the DFI is not too much influenced by $\delta J = 0.1J$. Since experimentally realized coupling variations are typically below 5% [103,104], coupling disorder is unlikely to constitute a major limitation in practice.

We finally note that giant atoms can also be realized in cold-atom systems [37], where strong photon-photon interactions can be engineered via Rydberg blockade [105,106]. For this platform, further analysis is required to determine how feasible it would be to observe and control doublon BICs.

VI. CONCLUSION AND OUTLOOK

We have introduced giant atoms coupled to nonlinear structured waveguides as a platform to realize many-body bound states in the continuum, leveraging the destructive interference between spatially separated emission pathways—an effect unique to GAs. We first numerically demonstrated the

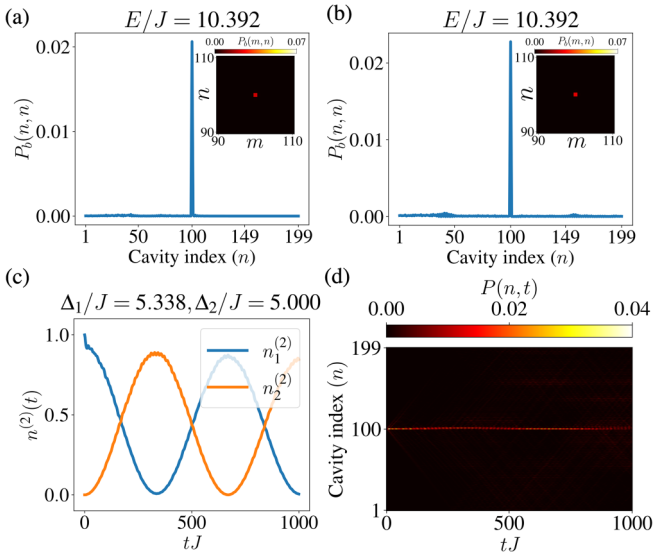


FIG. 6. Effect of intercavity coupling disorder on doublon BICs and DFI dynamics. (a), (b) Doublon BICs for coupling-disorder strengths $\delta J = 0.2J$ and $0.1J$, respectively. (c), (d) DFI dynamics for $\delta J = 0.1J$. Other parameters are the same as in Fig. 3(a).

formation of doublon BICs in setups with direct two-photon emission to the waveguide and showed that these BICs can mediate decoherence-free interactions between different GAs. We then extended our analysis to the more experimentally relevant case where only single-photon emission is allowed and found that doublon BICs and their associated DFIs still emerge, enabled by virtual two-photon transitions. These findings highlight interference as a powerful mechanism for realizing many-body BICs and put forward GAs as a versatile platform for engineering docoherence-free interactions mediated by two- and many-body BICs.

The nonradiative nature of doublon BICs makes them promising candidates for entangled-state preparation [44] and fault-tolerant quantum gates in noisy environments [63,107–109]. Their intrinsic many-body character enables applications beyond the single-excitation regime, such as preparing and distributing many-body entangled states [110–113], and implementing unconventional quantum gates involving more than one photon [114,115].

Looking ahead, the principles demonstrated here can be extended to $N \geqslant 2$ many-body BICs [29] in GAs with more levels. However, we note that a more precise frequency tuning is required then, as the bandwidth for many-body bound states become narrower as N increases. Also, analytical and numerical treatments become more challenging here, as the Hilbert-space dimension rapidly grows with N. The interplay between photon-photon interactions and interference thus opens a rich frontier for both theoretical and experimental exploration of many-body BICs. Finally, our strategy is not limited to bosonic systems such as the Bose-Hubbard model, but can also be extended to interacting fermionic systems. Examples include two-magnon bound states in Ising-like XXZ chains [116–118], two-fermion bound states in the one-dimensional Fermi-Hubbard model [119], and more complex many-body excitations such as Cooper pairs.

ACKNOWLEDGMENTS

We thank Ariadna Soro and Xin Wang for fruitful discussions. G.C. was supported by the European Union's Horizon Europe program HORIZON-MSCA-2023-PF-01-01 via Project No. 101146565 (SING-ATOM). A.F.K. acknowledges support from the Swedish Foundation for Strategic Research (Grants No. FFL21-0279 and No. FUS21-0063), the Horizon Europe program HORIZON-CL4-2022-QUANTUM-01-SGA via Project No. 101113946 OpenSuperQPlus100, and from the Knut and Alice Wallenberg Foundation through the Wallenberg Centre for Quantum Technology (WACQT).

DATA AVAILABILITY

The code used in this work and the data that support the findings of this article are openly available at GitHub [120].

APPENDIX A: NUMERICAL DETAILS

In the main text, we defined the full Hamiltonian of the system (N_a giant atoms interacting with a waveguide consisting of N cavities at p_n coupling points for atom n) in Eqs. (1), (2), (4), and (9) (for the excitation-number-conserving interaction Hamiltonian $H_{\rm int}$):

$$H = H_A + H_B + H_{\rm int}, \tag{A1}$$

$$H_A = \sum_{n=1}^{N_a}\left[(\Delta_2+\Delta_1)\frac{\sigma_n^{(2),+}\sigma_n^{(2),-}}{2} + \Delta_1\sigma_n^{(1),+}\sigma_n^{(1),-}\right], \tag{A2}$$

$$H_B = \sum_{n=1}^{N}\frac{U}{2}a_n^\dagger a_n^\dagger a_n a_n - \sum_{n=1}^{N-1}J(a_n^\dagger a_{n+1} + \text{H.c.}), \tag{A3}$$

$$H_{\rm int} = g\sum_{n=1}^{N_a}\sum_{j=1}^{p_n}\left[\sigma_n^{(1),+}a_{x_{nj}} + \sigma_n^{(2),+}a_{x_{nj}} + \text{H.c.}\right]. \tag{A4}$$

To perform numerical simulations for time evolution of the system with $N_a = 2$ giant atoms under this Hamiltonian, we first identify a complete basis for the system in the two-excitation subspace by enumerating all physically distinct states associated with each number of atomic excitations in this subspace:

(1) For two atomic excitations and no photons, there are three distinct states: $|02,00\rangle$, $|20,00\rangle$, and $|11,00\rangle$.

(2) For one atomic excitation and one photon in the waveguide, there are $2N$ states: $|10,n0\rangle$ and $|01,n0\rangle$ for each mode index n.

(3) For no atomic excitations and two photons in the waveguide, we have $N(N+1)/2$ states of the form $|00,nm\rangle$, where $|00,nm\rangle \equiv |00,mn\rangle$ enforces symmetry under exchange.

The basis states here are explicitly defined as

$$|20,00\rangle = \frac{\sigma_1^{(2),+}\sigma_1^{(1),+}}{\sqrt{2}}|\text{vac}\rangle, \quad |02,00\rangle = \frac{\sigma_2^{(2),+}\sigma_2^{(1),+}}{\sqrt{2}}|\text{vac}\rangle,$$
$$|11,00\rangle = \sigma_1^{(1),+}\sigma_2^{(1),+}|\text{vac}\rangle, \quad |10,n0\rangle = \sigma_1^{(1),+}a_n^\dagger|\text{vac}\rangle,$$
$$|01,n0\rangle = \sigma_2^{(1),+}a_n^\dagger|\text{vac}\rangle, \qquad |00,nm\rangle = a_n^\dagger a_m^\dagger|\text{vac}\rangle. \tag{A5}$$

Matrix elements of the Hamiltonian are computed by evaluating inner products between basis states and the Hamiltonian operator. For example,

$$\langle 20,00|H|20,00\rangle = \langle 20,00|H_A|20,00\rangle = \Delta_2 + \Delta_1. \quad \text{(A6)}$$

We use Algorithm 1 to construct the Hamiltonian matrix numerically. By diagonalizing the constructed Hamiltonian, we obtain its eigenvalues and vectors. We then use the inverse participation ratio (IPR) to identify highly localized states that potentially are bound states in the continuum. The IPR for a state $|\psi\rangle$ is defined as [79]

$$\mathrm{IPR}(|\psi\rangle) = \sum_n |\psi_n|^4, \quad \text{(A7)}$$

where ψ_n is the amplitude of the nth basis state of the Hamiltonian. A value of IPR ≈ 1 indicates a highly localized state, while IPR $\approx 1/\sqrt{N}$ suggests a delocalized state. The BICs can therefore be found by locating the eigenstates that have the highest IPR values. In systems where BICs exist, the eigenstate with either the largest or second largest IPR typically corresponds to the BIC.

APPENDIX B: ANALYTICAL DERIVATION

Here, we derive the effective Hamiltonian H_{eff} for a single giant atom coupled at two points to the structured waveguide with the excitation-number-conserving interaction Hamiltonian H_{int} given in Eq. (9), such that Eqs. (A2)–(A4) are simplified to

$$\begin{aligned} H_A &= \left[(\Delta_2+\Delta_1)\sigma^{(2),+}\sigma^{(2),-} + \Delta_1\sigma^{(1),+}\sigma^{(1),-}\right], \\ H_B &= \sum_{n=1}^{N}\frac{U}{2}a_n^\dagger a_n^\dagger a_n a_n - \sum_{n=1}^{N-1} J(a_n^\dagger a_{n+1} + \mathrm{H.c.}), \\ H_{\mathrm{int}} &= g\sum_{j=1}^{2}\left[\sigma^{(1),+}a_{x_j} + \sigma^{(2),+}a_{x_j} + \mathrm{H.c.}\right], \end{aligned} \quad \text{(B1)}$$

where $x_{1,2}$ are the coupling-point coordinates of the atom. In particular, we are interested in the regime where the energy of the $|2\rangle$ level of the atom lies within the doublon band: $\Delta_1 + \Delta_2 \approx \omega_D(k)$. We therefore derive the effective Hamiltonian in the subspace spanned by the states $|2\rangle$ and $|\psi_D(k)\rangle$.

Since H_{int} does not directly couple these states (i.e., $\langle\psi_D(k)|H_{\mathrm{int}}|2\rangle = 0$), the lowest nonzero contribution arises from second-order perturbation theory:

$$\langle\psi_D(k)|H_{\mathrm{eff}}|2\rangle = \sum_m \frac{\langle\psi_D(k)|H_{\mathrm{int}}|m\rangle\langle m|H_{\mathrm{int}}|2\rangle}{\Delta_1+\Delta_2-E_m}, \quad \text{(B2)}$$

where $|m\rangle$ are eigenstates of $H_A + H_B$. To yield a nonzero contribution, both matrix elements in the numerator must be nonzero. The only such intermediate states $|m\rangle$ are $|1,k'\rangle = \sigma^{(1),+}a_{k'}^\dagger|\mathrm{vac}\rangle$ with $E(k') = \Delta_1 + 2J\cos k'$.

We first Fourier transform the interaction Hamiltonian:

$$H_{\mathrm{int}} = \frac{g}{\sqrt{N}}\sum_{j=1}^{2}\sum_k [\sigma^{(1),+} + \sigma^{(2),+}]\exp(ikx_j)a_k + \mathrm{H.c.}, \quad \text{(B3)}$$

which gives

$$\langle 1,k'|H_{\mathrm{int}}|2\rangle = \frac{\sqrt{2}g}{\sqrt{N}}\sum_{j=1}^{2}\exp(ik'x_j) := G(k'). \quad \text{(B4)}$$

To evaluate $\langle\psi_D(k)|H_{\mathrm{int}}|1,k'\rangle$, we note that

$$|\psi_D(k)\rangle = \frac{1}{\sqrt{2}}\sum_{m=1}^{N}\sum_{n=1}^{N} e^{ik\frac{(m+n)}{2}}e^{-\frac{|m-n|}{\varsigma(k)}}a_m^\dagger a_n^\dagger|\mathrm{vac}\rangle, \quad \text{(B5)}$$

where the localization length $\varsigma(k)$ is given by [121]

$$\varsigma(k) = -\left[\ln\left(\frac{\sqrt{U^2+16J^2\cos(k/2)^2}-U}{4J\cos(k/2)}\right)\right]^{-1}. \quad \text{(B6)}$$

For large U, such as $U = 10J$ considered in the main text, the localization length $\varsigma(k)$ is sufficiently small [e.g., $\varsigma(\pi/2) \approx 0.506$] that we can approximate $\exp[-\frac{|m-n|}{\varsigma(k)}]$ as δ_{mn}, yielding

$$|\psi_D(k)\rangle = \frac{1}{\sqrt{2}}\sum_{n=1}^{N}\exp(ikn)a_n^\dagger a_n^\dagger|\mathrm{vac}\rangle \quad \text{(B7)}$$

and

$$\langle\psi_D(k)|H_{\mathrm{int}}|1,k'\rangle = G^*(k-k'). \quad \text{(B8)}$$

Therefore, the second-order matrix element becomes

$$\begin{aligned} &\langle\psi_D(k)|H_{\mathrm{eff}}|2\rangle \\ &= \sum_{k'}\frac{1}{\Delta_2-2J\cos k'}G(k-k')G(k') \\ &= \frac{2g^2}{N}\sum_{k'}\frac{e^{ikx_1}+e^{ikx_2}}{\Delta_2-2J\cos k'} \\ &\quad + \frac{2g^2}{N}\sum_{k'}\frac{e^{ikx_1}e^{ik'(x_2-x_1)}+e^{ikx_2}e^{ik'(x_1-x_2)}}{\Delta_2-2J\cos k'}. \end{aligned} \quad \text{(B9)}$$

Due to the oscillation in k', the second term is suppressed, and the first term in Eq. (B9) dominates. In particular, at the decoherence-free wave vector $k = \pi/(x_2-x_1)$, the second term vanishes. This yields

$$\langle\psi_D(k)|H_{\mathrm{eff}}|2\rangle = g_{\mathrm{eff}}\sum_{j=1}^{2}\exp(ikx_j), \quad \text{(B10)}$$

where

$$g_{\mathrm{eff}} = \frac{2g^2}{N}\sum_{k'}\frac{1}{\Delta_2-2J\cos k'}. \quad \text{(B11)}$$

For the parameters used in Figs. 3(a)–3(d) ($N = 199$, $U = 10J$, $g = 0.25J$, $\Delta_2 = 5J$, and $x_2 - x_1 = 2$), this effective coupling takes a value of $g_{\mathrm{eff}} \approx 0.027J$.

ALGORITHM 1. Construct Hamiltonian.

Let $D = \binom{N+N_a+1}{2}$;
Initialize $H \in \mathbb{C}^{D\times D}$ with zeros, $g[i][j]$ as the coupling strength of atom i at coupling point j, couplePoints[i] as the coupling point indices of atom i, and $\Delta_{1(2)}[i]$ as the level spacing associated with level 1(2).
for $i = 0$ **to** $\binom{N_a+1}{2} - 1$ **do**
  if $i < N_a$ **then**
    $H[i,i] = \Delta_1[i] + \Delta_2[i]$;
    foreach *couplePoint, k in couplePoints*[i] **do**
      $j = \binom{N_a+1}{2} + iN + (\text{couplePoint} - 1)$;
      $H[i,j] = \sqrt{2}g[i][k]$;
  else
    foreach $0 \le j < k < N_a$ **do**
      if $i == jN - j(j-1)/2 + k - j$ **then**
        $H[i,i] = \Delta_1[j] + \Delta_1[k]$
for $i = 0$ **to** $N_a - 2$ **do**
  for $j = i+1$ **to** $N_a - 1$ **do**
    $\text{index} = (i+1)N_a - i(i-1)/2 + j - 2i - 1$;
    foreach *(couplePoint, k) in couplePoints*[i] **do**
      $H[\text{index}, \binom{N_a+1}{2} + jN + \text{couplePoint} - 1] = g[i][k]$;
    foreach *(couplePoint, k) in couplePoints[j])* **do**
      $H[\text{index}, \binom{N_a+1}{2} + iN + \text{couplePoint} - 1] = g[i][k]$;
for $i = 0$ **to** $N_a - 1$ **do**
  for $j = 0$ **to** $N - 1$ **do**
    $\text{index} = \binom{N_a+1}{2} + iN + j$;
    $H[\text{index}, \text{index}] = \Delta_1[i]$;
    if $j \neq N-1$ **then**
      $H[\text{index}, \text{index}+1] = -J$;
    iter $= 0$;
    foreach *couplePoint in couplePoints*[i] **do**
      $k = \text{couplePoint} - 1$;
      if $j \le k$ **then**
        $c_k = jN - j(j-1)/2 + k - j$;
      else
        $c_k = kN - k(k-1)/2 + j - k$;
      $H[\text{index}, c_k + \binom{N_a+1}{2} + NN_a] = g[i][\text{iter}]$
      if $j == k$ **then**
        $H[i, c_k + \binom{N_a+1}{2} + NN_a] = g_{\text{DC}}[i][\text{iter}]$;
        $H[\text{index}, c_k + \binom{N_a+1}{2} + NN_a] = \sqrt{2} \cdot g[i][\text{iter}]$;
      iter++
for $i = 0$ **to** $\binom{N+1}{2} - 1$ **do**
  $\text{index} = i + \binom{N_a+1}{2} + N_a N$;
  for $k = 0$ **to** $N - 1$ **do**
    if $i < kN - k(k-1)/2$ **then**
      $c_k = i - N(k-1) + \frac{(k-2)(k-1)}{2} + (k-1)$, $c_j = k - 1$; break;
    else
      $c_k = N - 1$, $c_j = N - 1$;
  foreach *valid neighbor* (j', k') **do**
    $c_{jk} = Nj' - j'(j'-1)/2 + k' - j'; \binom{N_a+1}{2} + N_{aN}$
    if $j' = k'$ **then**
      $H[\text{index}, c_{jk}] = -\sqrt{2}J$;
      $H[c_{jk}, c_{jk}] = U$;
    else
      $H[\text{index}, c_{jk}] = -J$;

Expression (B10) mirrors the single-photon matrix element

$$\langle \text{vac}|a_k H_{\text{int}}|1\rangle = g\sum_{j=1}^{2}\exp(ikx_j), \tag{B12}$$

except with $g \to g_{\text{eff}}$. The factor $\sum_{j=1}^{2}\exp(ikx_j)$, characteristic of giant atoms, gives rise to interference effects and underpins both bound states in the continuum and decoherence-free interactions.

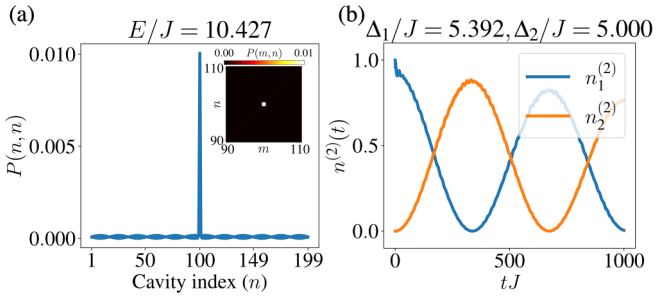


FIG. 7. Doublon BIC and DFI without accounting for the Lamb shift of the $|2\rangle$ level for $U = 10J$, $g = 0.25J$, $\Delta x = 2$, $\Delta_1 = 5.392J$, and $\Delta_2 = 5J$. (a) The doublon BIC for a single giant atom, where an extension of the bound state wavefunction outside the coupling points (99 and 101) can be seen, indicating that it is not a perfect bound state. (b) The corresponding DFI dynamics for two giant atoms, where the dynamics show a gradual decay of the total atomic population, due to the imperfect BIC.

In addition to the effective coupling, the second-order correction also induces a Lamb shift Δ_{Lamb} in the $|2\rangle$ level:

$$\begin{aligned}\langle 2|H_{\text{eff}}|2\rangle &= \sum_{k'} \frac{G(k')G^*(k')}{\Delta_2 - 2J\cos k'} \\ &= \frac{2g^2}{N}\sum_{k'} \frac{1}{\Delta_2 - 2J\cos k'}\left|\sum_{j=1}^{2}\exp(ik'x_j)\right|^2 \\ &= \frac{2g^2}{N}\sum_{k'} \frac{2+2\cos[k'(x_2-x_1)]}{\Delta_2 - 2J\cos k'}. \end{aligned} \tag{B13}$$

For the parameters used in Figs. 3(a)–3(d), this Lamb shift takes a value of $\Delta_{\text{Lamb}} \approx 0.057J$.

Finally, the doublon modes also get perturbed by H_{int}:

$$\begin{aligned}&\langle\psi_D(k_1)|H_{\text{eff}}|\psi_D(k_2)\rangle \\ &= \sum_{k'} \frac{G^*(k_1-k')G(k_2-k')}{\Delta_2 - 2J\cos k'} \\ &= \frac{2g^2}{N}\sum_{k'} \frac{e^{i(k_2-k_1)x_1} + e^{i(k_2-k_1)x_2}}{\Delta_2 - 2J\cos k'} \\ &\quad + \frac{2g^2}{N}\sum_{k'} \frac{e^{i(k_2-k_1)x_1}e^{i(k_2-k')(x_2-x_1)}}{\Delta_2 - 2J\cos k'} \\ &\quad + \frac{2g^2}{N}\sum_{k'} \frac{e^{i(k_2-k_1)x_2}e^{i(k_2-k')(x_1-x_2)}}{\Delta_2 - 2J\cos k'}, \end{aligned} \tag{B14}$$

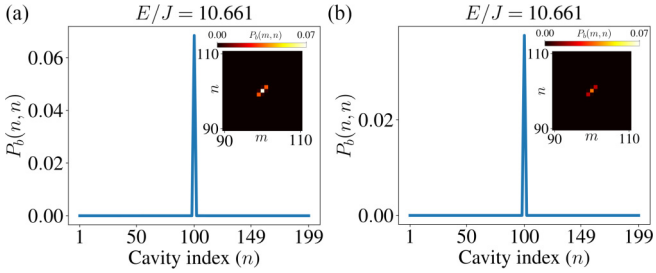


FIG. 8. Doublon BICs for a coupling-point separation $\Delta x = 4$, in the cases of (a) direct two-photon emission and (b) single-photon coupling. Other parameters are the same as in Figs. 2(a) and 3(a), respectively.

which modifies both the doublon dispersion and the doublon eigenstates.

As a result, the decoherence-free condition also changes: satisfying $\Delta_1 + \Delta_2 = \omega_{\text{DF}}$ is no longer sufficient. The corrected condition becomes

$$\Delta_1 + \Delta_2 + \Delta_{\text{Lamb}} = \omega_{\text{DF}} + \Delta_D(\omega_{\text{DF}}), \tag{B15}$$

where $\Delta_D(\omega_{\text{DF}})$ is the perturbative shift in the doublon energy.

As shown in Fig. 7, choosing $\Delta_1 + \Delta_2 = \omega_{\text{DF}}$ fails to produce a true BIC: The state energy is shifted, and the wavefunction spreads beyond the coupling region [Fig. 7(a)]. Correspondingly, the DFI quality deteriorates [Fig. 7(b)].

Numerically, we find that setting $\Delta_1 + \Delta_2 + \Delta = \omega_{\text{DF}}$ with $\Delta = 0.054J$ results in the best decoherence-free quality for the parameters in Fig 3. The close match between Δ and Δ_{Lamb} indicates that H_{int} only has a minor effect on the doublon dispersion.

APPENDIX C: LARGER SPACING

We show the doublon BICs for a larger spacing of $\Delta x = 4$ for direct two-photon emission [Fig. 8(a)] and single-photon coupling [Fig. 8(b)], with $U/J = 10$. Similar to Figs. 2(a) and 3(a), where $\Delta x = 2$, these bound states are confined between the coupling points, and their energies lie within the continuum. This highlights that our mechanism also works for larger spacings.

[1] J. von Neumann and E. P. Wigner, Über merkwürdige diskrete Eigenwerte, in *The Collected Works of Eugene Paul Wigner* (Springer, Berlin, 1993), pp. 291–293.
[2] F. H. Stillinger and D. R. Herrick, Bound states in the continuum, Phys. Rev. A **11**, 446 (1975).
[3] Y. Plotnik, O. Peleg, F. Dreisow, M. Heinrich, S. Nolte, A. Szameit, and M. Segev, Experimental observation of optical bound states in the continuum, Phys. Rev. Lett. **107**, 183901 (2011).
[4] M. Robnik, A simple separable Hamiltonian having bound states in the continuum, J. Phys. A: Math. Gen. **19**, 3845 (1986).
[5] H. Friedrich and D. Wintgen, Interfering resonances and bound states in the continuum, Phys. Rev. A **32**, 3231 (1985).
[6] D. C. Marinica, A. G. Borisov, and S. V. Shabanov, Bound states in the continuum in photonics, Phys. Rev. Lett. **100**, 183902 (2008).

[7] Y. Yang, C. Peng, Y. Liang, Z. Li, and S. Noda, Analytical perspective for bound states in the continuum in photonic crystal slabs, Phys. Rev. Lett. **113**, 037401 (2014).

[8] C. W. Hsu, B. Zhen, A. Douglas Stone, J. D. Joannopoulos, and M. Soljačić, Bound states in the continuum, Nat. Rev. Mater. **1**, 16048 (2016).

[9] K. Koshelev, A. Bogdanov, and Y. Kivshar, Engineering with bound states in the continuum, Opt. Photon. News **31**, 38 (2020).

[10] S. Joseph, S. Pandey, S. Sarkar, and J. Joseph, Bound states in the continuum in resonant nanostructures: An overview of engineered materials for tailored applications, Nanophoton. **10**, 4175 (2021).

[11] S. I. Azzam and A. V. Kildishev, Photonic bound states in the continuum: From basics to applications, Adv. Opt. Mater. **9**, 2001469 (2021).

[12] I. Deriy, I. Toftul, M. Petrov, and A. Bogdanov, Bound states in the continuum in compact acoustic resonators, Phys. Rev. Lett. **128**, 084301 (2022).

[13] H. Tong, S. Liu, M. Zhao, and K. Fang, Observation of phonon trapping in the continuum with topological charges, Nat. Commun. **11**, 5216 (2020).

[14] L. Carletti, K. Koshelev, C. De Angelis, and Y. Kivshar, Giant nonlinear response at the nanoscale driven by bound states in the continuum, Phys. Rev. Lett. **121**, 033903 (2018).

[15] Z. Liu, Y. Xu, Y. Lin, J. Xiang, T. Feng, Q. Cao, J. Li, S. Lan, and J. Liu, High-Q quasibound states in the continuum for nonlinear metasurfaces, Phys. Rev. Lett. **123**, 253901 (2019).

[16] K. Koshelev, Y. Tang, K. Li, D.-Y. Choi, G. Li, and Y. Kivshar, Nonlinear metasurfaces governed by bound states in the continuum, ACS Photon. **6**, 1639 (2019).

[17] L. Carletti, S. S. Kruk, A. A. Bogdanov, C. De Angelis, and Y. Kivshar, High-harmonic generation at the nanoscale boosted by bound states in the continuum, Phys. Rev. Res. **1**, 023016 (2019).

[18] A. P. Anthur, H. Zhang, R. Paniagua-Dominguez, D. A. Kalashnikov, S. T. Ha, T. W. W. Maß, A. I. Kuznetsov, and L. Krivitsky, Continuous wave second harmonic generation enabled by quasi-bound-states in the continuum on gallium phosphide metasurfaces, Nano Lett. **20**, 8745 (2020).

[19] G. Zograf, K. Koshelev, A. Zalogina, V. Korolev, R. Hollinger, D.-Y. Choi, M. Zuerch, C. Spielmann, B. Luther-Davies, D. Kartashov, S. V. Makarov, S. S. Kruk, and Y. Kivshar, High-harmonic generation from resonant dielectric metasurfaces empowered by bound states in the continuum, ACS Photon. **9**, 567 (2022).

[20] A. Kodigala, T. Lepetit, Q. Gu, B. Bahari, Y. Fainman, and B. Kanté, Lasing action from photonic bound states in continuum, Nature (London) **541**, 196 (2017).

[21] S. T. Ha, Y. H. Fu, N. K. Emani, Z. Pan, R. M. Bakker, R. Paniagua-Domínguez, and A. I. Kuznetsov, Directional lasing in resonant semiconductor nanoantenna arrays, Nat. Nanotechnol. **13**, 1042 (2018).

[22] M. Wu, S. T. Ha, S. Shendre, E. G. Durmusoglu, W.-K. Koh, D. R. Abujetas, J. A. Sánchez-Gil, R. Paniagua-Domínguez, H. V. Demir, and A. I. Kuznetsov, Room-temperature lasing in colloidal nanoplatelets via Mie-resonant bound states in the continuum, Nano Lett. **20**, 6005 (2020).

[23] Y. Wang, Y. Fan, X. Zhang, H. Tang, Q. Song, J. Han, and S. Xiao, Highly controllable etchless perovskite microlasers based on bound states in the continuum, ACS Nano **15**, 7386 (2021).

[24] F. Yesilkoy, E. R. Arvelo, Y. Jahani, M. Liu, A. Tittl, V. Cevher, Y. Kivshar, and H. Altug, Ultrasensitive hyperspectral imaging and biodetection enabled by dielectric metasurfaces, Nat. Photon. **13**, 390 (2019).

[25] S. Romano, G. Zito, S. N. L. Yépez, S. Cabrini, E. Penzo, G. Coppola, I. Rendina, and V. Mocellaark, Tuning the exponential sensitivity of a bound-state-in-continuum optical sensor, Opt. Express **27**, 18776 (2019).

[26] M. L. Tseng, Y. Jahani, A. Leitis, and H. Altug, Dielectric metasurfaces enabling advanced optical biosensors, ACS Photon. **8**, 47 (2021).

[27] H. Altug, S.-H. Oh, S. A. Maier, and J. Homola, Advances and applications of nanophotonic biosensors, Nat. Nanotechnol. **17**, 5 (2022).

[28] Y. Chen, C. Zhao, Y. Zhang, and C.-W. Qiu, Integrated molar chiral sensing based on high- Q metasurface, Nano Lett. **20**, 8696 (2020).

[29] S. Sugimoto, Y. Ashida, and M. Ueda, Many-body bound states in the continuum, arXiv:2307.05456.

[30] J. M. Zhang, D. Braak, and M. Kollar, Bound states in the continuum realized in the one-dimensional two-particle Hubbard model with an impurity, Phys. Rev. Lett. **109**, 116405 (2012).

[31] Y. Ashida, T. Yokota, A. İmamoğlu, and E. Demler, Nonperturbative waveguide quantum electrodynamics, Phys. Rev. Res. **4**, 023194 (2022).

[32] N. Sun, W. Zhang, H. Yuan, and X. Zhang, Boundary-localized many-body bound states in the continuum, Commun. Phys. **7**, 299 (2024).

[33] A. F. Kockum, Quantum optics with giant atoms - the first five years, in *International Symposium on Mathematics, Quantum Theory, and Cryptography*, edited by T. Takagi, M. Wakayama, K. Tanaka, N. Kunihiro, K. Kimoto, and Y. Ikematsu, Mathematics for Industry Vol. 33 (Springer, Singapore, 2021), pp. 125–146.

[34] A. Frisk Kockum, P. Delsing, and G. Johansson, Designing frequency-dependent relaxation rates and Lamb shifts for a giant artificial atom, Phys. Rev. A **90**, 013837 (2014).

[35] L. Guo, A. L. Grimsmo, A. F. Kockum, M. Pletyukhov, and G. Johansson, Giant acoustic atom: A single quantum system with a deterministic time delay, Phys. Rev. A **95**, 053821 (2017).

[36] A. F. Kockum, G. Johansson, and F. Nori, Decoherence-free interaction between giant atoms in waveguide quantum electrodynamics, Phys. Rev. Lett. **120**, 140404 (2018).

[37] A. González-Tudela, C. Sánchez Muñoz, and J. I. Cirac, Engineering and harnessing giant atoms in high-dimensional baths: A proposal for implementation with cold atoms, Phys. Rev. Lett. **122**, 203603 (2019).

[38] L. Guo, A. F. Kockum, F. Marquardt, and G. Johansson, Oscillating bound states for a giant atom, Phys. Rev. Res. **2**, 043014 (2020).

[39] P. O. Guimond, B. Vermersch, M. L. Juan, A. Sharafiev, G. Kirchmair, and P. Zoller, A unidirectional on-chip photonic interface for superconducting circuits, npj Quantum Inf. **6**, 32 (2020).

[40] A. Ask, Y.-L. L. Fang, and A. F. Kockum, Synthesizing electromagnetically induced transparency without a con-

trol field in waveguide QED using small and giant atoms, arXiv:2011.15077.

[41] D. Cilluffo, A. Carollo, S. Lorenzo, J. A. Gross, G. M. Palma, and F. Ciccarello, Collisional picture of quantum optics with giant emitters, Phys. Rev. Res. **2**, 043070 (2020).

[42] X. Wang, T. Liu, A. F. Kockum, H.-R. Li, and F. Nori, Tunable chiral bound states with giant atoms, Phys. Rev. Lett. **126**, 043602 (2021).

[43] L. Du and Y. Li, Single-photon frequency conversion via a giant Λ-type atom, Phys. Rev. A **104**, 023712 (2021).

[44] A. Soro and A. F. Kockum, Chiral quantum optics with giant atoms, Phys. Rev. A **105**, 023712 (2022).

[45] X. Wang and H.-R. Li, Chiral quantum network with giant atoms, Quantum Sci. Technol. **7**, 035007 (2022).

[46] L. Du, Y. Zhang, J. H. Wu, A. F. Kockum, and Y. Li, Giant atoms in a synthetic frequency dimension, Phys. Rev. Lett. **128**, 223602 (2022).

[47] L. Du, Y.-T. Chen, Y. Zhang, and Y. Li, Giant atoms with time-dependent couplings, Phys. Rev. Res. **4**, 023198 (2022).

[48] S. Terradas-Briansó, C. A. González-Gutiérrez, F. Nori, L. Martín-Moreno, and D. Zueco, Ultrastrong waveguide QED with giant atoms, Phys. Rev. A **106**, 063717 (2022).

[49] A. Soro, C. S. Muñoz, and A. F. Kockum, Interaction between giant atoms in a one-dimensional structured environment, Phys. Rev. A **107**, 013710 (2023).

[50] L. Du, L. Guo, Y. Zhang, and A. F. Kockum, Giant emitters in a structured bath with non-Hermitian skin effect, Phys. Rev. Res. **5**, L042040 (2023).

[51] E. R. Ingelsten, A. F. Kockum, and A. Soro, Avoiding decoherence with giant atoms in a two-dimensional structured environment, Phys. Rev. Res. **6**, 043222 (2024).

[52] L. Leonforte, X. Sun, D. Valenti, B. Spagnolo, F. Illuminati, A. Carollo, and F. Ciccarello, Quantum optics with giant atoms in a structured photonic bath, Quantum Sci. Technol. **10**, 015057 (2025).

[53] X. Wang, H.-B. Zhu, T. Liu, and F. Nori, Realizing quantum optics in structured environments with giant atoms, Phys. Rev. Res. **6**, 013279 (2024).

[54] F. Roccati and D. Cilluffo, Controlling Markovianity with chiral giant atoms, Phys. Rev. Lett. **133**, 063603 (2024).

[55] R.-Y. Gong, Z.-Y. He, C.-H. Yu, G.-F. Zhang, F. Nori, and Z.-L. Xiang, Tunable quantum router with giant atoms, implementing quantum gates, teleportation, non-reciprocity, and circulators, arXiv:2411.19307.

[56] L. Du and A. F. Kockum, Unconventional and robust light-matter interactions based on the non-Hermitian skin effect, Phys. Rev. Res. **7**, 013140 (2025).

[57] L. Du, X. Wang, A. F. Kockum, and J. Splettstoesser, Dressed interference in giant superatoms: Entanglement generation and transfer, Phys. Rev. Lett. **135**, 223601 (2025).

[58] M. V. Gustafsson, T. Aref, A. F. Kockum, M. K. Ekström, G. Johansson, and P. Delsing, Propagating phonons coupled to an artificial atom, Science **346**, 207 (2014).

[59] R. Manenti, A. F. Kockum, A. Patterson, T. Behrle, J. Rahamim, G. Tancredi, F. Nori, and P. J. Leek, Circuit quantum acoustodynamics with surface acoustic waves, Nat. Commun. **8**, 975 (2017).

[60] K. J. Satzinger, Y. P. Zhong, H.-S. Chang, G. A. Peairs, A. Bienfait, M.-H. Chou, A. Y. Cleland, C. R. Conner, É. Dumur, J. Grebel, I. Gutierrez, B. H. November, R. G. Povey, S. J. Whiteley, D. D. Awschalom, D. I. Schuster, and A. N. Cleland, Quantum control of surface acoustic-wave phonons, Nature (London) **563**, 661 (2018).

[61] A. Bienfait, K. J. Satzinger, Y. P. Zhong, H.-S. Chang, M.-H. Chou, C. R. Conner, É. Dumur, J. Grebel, G. A. Peairs, R. G. Povey, and A. N. Cleland, Phonon-mediated quantum state transfer and remote qubit entanglement, Science **364**, 368 (2019).

[62] G. Andersson, B. Suri, L. Guo, T. Aref, and P. Delsing, Non-exponential decay of a giant artificial atom, Nat. Phys. **15**, 1123 (2019).

[63] B. Kannan, M. J. Ruckriegel, D. L. Campbell, A. Frisk Kockum, J. Braumüller, D. K. Kim, M. Kjaergaard, P. Krantz, A. Melville, B. M. Niedzielski, A. Vepsäläinen, R. Winik, J. L. Yoder, F. Nori, T. P. Orlando, S. Gustavsson, and W. D. Oliver, Waveguide quantum electrodynamics with superconducting artificial giant atoms, Nature (London) **583**, 775 (2020).

[64] A. Bienfait, Y. P. Zhong, H.-S. Chang, M.-H. Chou, C. R. Conner, É. Dumur, J. Grebel, G. A. Peairs, R. G. Povey, K. J. Satzinger, and A. N. Cleland, Quantum erasure using entangled surface acoustic phonons, Phys. Rev. X **10**, 021055 (2020).

[65] G. Andersson, M. K. Ekström, and P. Delsing, Electromagnetically induced acoustic transparency with a superconducting circuit, Phys. Rev. Lett. **124**, 240402 (2020).

[66] A. M. Vadiraj, A. Ask, T. G. McConkey, I. Nsanzineza, C. W. S. Chang, A. F. Kockum, and C. M. Wilson, Engineering the level structure of a giant artificial atom in waveguide quantum electrodynamics, Phys. Rev. A **103**, 023710 (2021).

[67] Z. Q. Wang, Y. P. Wang, J. Yao, R. C. Shen, W. J. Wu, J. Qian, J. Li, S. Y. Zhu, and J. Q. You, Giant spin ensembles in waveguide magnonics, Nat. Commun. **13**, 7580 (2022).

[68] C. Joshi, F. Yang, and M. Mirhosseini, Resonance fluorescence of a chiral artificial atom, Phys. Rev. X **13**, 021039 (2023).

[69] J. Hu, D. Li, Y. Qie, Z. Yin, A. F. Kockum, F. Nori, and S. An, Engineering the environment of a superconducting qubit with an artificial giant atom, arXiv:2410.15377.

[70] A. Almanakly, B. Yankelevich, M. Hays, B. Kannan, R. Assouly, A. Greene, M. Gingras, B. M. Niedzielski, H. Stickler, M. E. Schwartz, K. Serniak, J. Î.-J. Wang, T. P. Orlando, S. Gustavsson, J. A. Grover, and W. D. Oliver, Deterministic remote entanglement using a chiral quantum interconnect, Nat. Phys. **21**, 825 (2025).

[71] V. Jouanny, L. Peyruchat, M. Scigliuzzo, A. Mercurio, E. Di Benedetto, D. De Bernardis, D. Sbroggiò, S. Frasca, V. Savona, F. Ciccarello, and P. Scarlino, Superstrong dynamics and directional emission of a giant atom in a structured bath, arXiv:2509.01579.

[72] S. Guo, Y. Wang, T. Purdy, and J. Taylor, Beyond spontaneous emission: Giant atom bounded in the continuum, Phys. Rev. A **102**, 033706 (2020).

[73] K. Winkler, G. Thalhammer, F. Lang, R. Grimm, J. Hecker Denschlag, A. J. Daley, A. Kantian, H. P. Büchler, and P. Zoller, Repulsively bound atom pairs in an optical lattice, Nature (London) **441**, 853 (2006).

[74] R. Piil and K. Mølmer, Tunneling couplings in discrete lattices, single-particle band structure, and eigenstates of interacting atom pairs, Phys. Rev. A **76**, 023607 (2007).

[75] Z. Wang, T. Jaako, P. Kirton, and P. Rabl, Supercorrelated radiance in nonlinear photonic waveguides, Phys. Rev. Lett. **124**, 213601 (2020).

[76] M. A. Gorlach and A. N. Poddubny, Topological edge states of bound photon pairs, Phys. Rev. A **95**, 053866 (2017).

[77] M. Ayyash, X. Xu, S. Ashhab, and M. Mariantoni, Driven multiphoton qubit-resonator interactions, Phys. Rev. A **110**, 053711 (2024).

[78] S. Felicetti, D. Z. Rossatto, E. Rico, E. Solano, and P. Forn-Díaz, Two-photon quantum Rabi model with superconducting circuits, Phys. Rev. A **97**, 013851 (2018).

[79] F. Wegner, Inverse participation ratio in $2 + \varepsilon$ dimensions, Z. Phys. B **36**, 209 (1980).

[80] See Appendixes for additional information on (1) the numerical details and (2) an analytical derivation of the effective model.

[81] S. John and J. Wang, Quantum electrodynamics near a photonic band gap: Photon bound states and dressed atoms, Phys. Rev. Lett. **64**, 2418 (1990).

[82] W. Rieck, A. Soro, A. F. Kockum, and G. Chen, Controlled-Z gates with giant atoms in structured waveguides, Phys. Rev. A **114**, 043719 (2026).

[83] J. Koch, T. M. Yu, J. Gambetta, A. A. Houck, D. I. Schuster, J. Majer, A. Blais, M. H. Devoret, S. M. Girvin, and R. J. Schoelkopf, Charge-insensitive qubit design derived from the Cooper pair box, Phys. Rev. A **76**, 042319 (2007).

[84] S. J. de Graaf, S. H. Xue, B. J. Chapman, J. D. Teoh, T. Tsunoda, P. Winkel, J. W. O. Garmon, K. M. Chang, L. Frunzio, S. Puri, and R. J. Schoelkopf, A mid-circuit erasure check on a dual-rail cavity qubit using the joint-photon number-splitting regime of circuit QED, npj Quantum Inf. **11**, 1 (2025).

[85] M. Scigliuzzo, L. Peyruchat, R. M. Marabini, C. Becker, V. Jouanny, P. Delsing, and P. Scarlino, Quantum acoustics with tunable nonlinearity in the superstrong coupling regime, PRX Quantum **7**, 010359 (2026).

[86] N. E. Frattini, R. G. Cortiñas, J. Venkatraman, X. Xiao, Q. Su, C. U. Lei, B. J. Chapman, V. R. Joshi, S. M. Girvin, R. J. Schoelkopf, S. Puri, and M. H. Devoret, Observation of pairwise level degeneracies and the quantum regime of the Arrhenius law in a double-well parametric oscillator, Phys. Rev. X **14**, 031040 (2024).

[87] S. Andersson, H. Havir, A. Ranni, S. Haldar, and V. F. Maisi, High-impedance microwave resonators with two-photon nonlinear effects, Nat. Commun. **16**, 552 (2025).

[88] A. Blais, A. L. Grimsmo, S. M. Girvin, and A. Wallraff, Circuit quantum electrodynamics, Rev. Mod. Phys. **93**, 025005 (2021).

[89] M. Kjaergaard, M. E. Schwartz, J. Braumüller, P. Krantz, J. I.-J. Wang, S. Gustavsson, and W. D. Oliver, Superconducting qubits: Current state of play, Annu. Rev. Condens. Matter Phys. **11**, 369 (2020).

[90] A. P. M. Place, L. V. H. Rodgers, P. Mundada, B. M. Smitham, M. Fitzpatrick, Z. Leng, A. Premkumar, J. Bryon, A. Vrajitoarea, S. Sussman, *et al.*, New material platform for superconducting transmon qubits with coherence times exceeding 0.3 milliseconds, Nat. Commun. **12**, 1779 (2021).

[91] A. Somoroff, Q. Ficheux, R. A. Mencia, H. Xiong, R. Kuzmin, and V. E. Manucharyan, Millisecond coherence in a superconducting qubit, Phys. Rev. Lett. **130**, 267001 (2023).

[92] Y. Kim, A. Eddins, S. Anand, K. X. Wei, E. van den Berg, S. Rosenblatt, H. Nayfeh, Y. Wu, M. Zaletel, K. Temme, and A. Kandala, Evidence for the utility of quantum computing before fault tolerance, Nature (London) **618**, 500 (2023).

[93] J. Biznárová, A. Osman, E. Rehnman, L. Chayanun, C. Križan, P. Malmberg, M. Rommel, C. Warren, P. Delsing, A. Yurgens, J. Bylander, and A. Fadavi Roudsari, Mitigation of interfacial dielectric loss in aluminum-on-silicon superconducting qubits, npj Quantum Inf. **10**, 78 (2024).

[94] S. Kono, J. Pan, M. Chegnizadeh, X. Wang, A. Youssefi, M. Scigliuzzo, and T. J. Kippenberg, Mechanically induced correlated errors on superconducting qubits with relaxation times exceeding 0.4 ms, Nat. Commun. **15**, 3950 (2024).

[95] M. Bal, A. A. Murthy, S. Zhu, F. Crisa, X. You, Z. Huang, T. Roy, J. Lee, D. v. Zanten, R. Pilipenko, *et al.*, Systematic improvements in transmon qubit coherence enabled by niobium surface encapsulation, npj Quantum Inf. **10**, 43 (2024).

[96] R. Acharya, D. A. Abanin, L. Aghababaie-Beni, I. Aleiner, T. I. Andersen, M. Ansmann, F. Arute, K. Arya, A. Asfaw, N. Astrakhantsev, *et al.*, Quantum error correction below the surface code threshold, Nature (London) **638**, 920 (2025).

[97] S. Poorgholam-Khanjari, V. Seferai, P. Foshat, C. Rose, H. Feng, R. H. Hadfield, M. Weides, and K. Delfanazari, Engineering high-Q superconducting tantalum microwave coplanar waveguide resonators for compact coherent quantum circuit, Sci. Rep. **15**, 27113 (2025).

[98] X. Wang, J. Howard, E. A. Sete, G. Stiehl, C. Kopas, S. Poletto, X. Wu, M. Field, N. Sharac, C. Eckberg, H. Cansizoglu, R. Katta, J. Mutus, A. Bestwick, K. Yadavalli, and D. P. Pappas, Precision frequency tuning of tunable transmon qubits using alternating-bias assisted annealing, in *2024 IEEE International Conference on Quantum Computing and Engineering (QCE), Montreal, QC, Canada*, (IEEE, Piscataway, NJ, 2024), pp. 1315–1323.

[99] C. Križan, M. Toselli, I. Ahmad, H. Khaksaran, M. Rommel, N. Trnjanin, J. Biznárová, M. Dahiya, E. Hogedal, H. Jakobsson, A. Nylander, J. Bylander, P. Delsing, and G. Tancredi, Electrical post-fabrication tuning of aluminum Josephson junctions at room temperature, Mater. Quantum Technol. **6**, 036001 (2026).

[100] A. Osman, J. Fernández-Pendás, C. Warren, S. Kosen, M. Scigliuzzo, A. Frisk Kockum, G. Tancredi, A. Fadavi Roudsari, and J. Bylander, Mitigation of frequency collisions in superconducting quantum processors, Phys. Rev. Res. **5**, 043001 (2023).

[101] X. Liu, W. Guo, Y. Wang, M. Dai, L. F. Wei, B. Dober, C. M. McKenney, G. C. Hilton, J. Hubmayr, J. E. Austermann, J. N. Ullom, J. Gao, and M. R. Vissers, Superconducting microresonator arrays with ideal frequency spacing, Appl. Phys. Lett. **111**, 252601 (2017).

[102] S. Schmidt and J. Koch, Circuit QED lattices: Towards quantum simulation with superconducting circuits, Ann. Phys. **525**, 395 (2013).

[103] B. Peropadre, D. Zueco, F. Wulschner, F. Deppe, A. Marx, R. Gross, and J. J. García-Ripoll, Tunable coupling engineering between superconducting resonators: From sidebands to effective gauge fields, Phys. Rev. B **87**, 134504 (2013).

[104] L. Frunzio, A. Wallraff, D. Schuster, J. Majer, and R. Schoelkopf, Fabrication and characterization of

superconducting circuit QED devices for quantum computation, IEEE Trans. Appl. Supercond. **15**, 860 (2005).
[105] A. V. Gorshkov, J. Otterbach, M. Fleischhauer, T. Pohl, and M. D. Lukin, Photon-photon interactions via Rydberg blockade, Phys. Rev. Lett. **107**, 133602 (2011).
[106] T. Peyronel, O. Firstenberg, Q.-Y. Liang, S. Hofferberth, A. V. Gorshkov, T. Pohl, M. D. Lukin, and V. Vuletić, Quantum nonlinear optics with single photons enabled by strongly interacting atoms, Nature (London) **488**, 57 (2012).
[107] G. Chen and A. F. Kockum, Simulating open quantum systems with giant atoms, Quantum Sci. Technol. **10**, 025028 (2025).
[108] G. Chen and A. F. Kockum, Scalable quantum simulator with an extended gate set in giant atoms, Quantum **10**, 1992 (2026).
[109] G. Chen and A. F. Kockum, Efficient three-qubit gates with giant atoms, arXiv:2510.04545.
[110] W. Dür, H. Aschauer, and H.-J. Briegel, Multiparticle entanglement purification for graph states, Phys. Rev. Lett. **91**, 107903 (2003).
[111] H.-J. Briegel, W. Dür, J. I. Cirac, and P. Zoller, Quantum repeaters: The role of imperfect local operations in quantum communication, Phys. Rev. Lett. **81**, 5932 (1998).
[112] S. Wehner, D. Elkouss, and R. Hanson, Quantum internet: A vision for the road ahead, Science **362**, eaam9288 (2018).
[113] N. Sangouard, C. Simon, H. de Riedmatten, and N. Gisin, Quantum repeaters based on atomic ensembles and linear optics, Rev. Mod. Phys. **83**, 33 (2011).
[114] T. Caneva, M. T. Manzoni, T. Shi, J. S. Douglas, J. I. Cirac, and D. E. Chang, Quantum dynamics of propagating photons with strong interactions: A generalized input–output formalism, New J. Phys. **17**, 113001 (2015).
[115] H. J. Kimble, The quantum internet, Nature (London) **453**, 1023 (2008).
[116] N. Papanicolaou and G. C. Psaltakis, Bethe ansatz for two-magnon bound states in anisotropic magnetic chains of arbitrary spin, Phys. Rev. B **35**, 342 (1987).
[117] N. Wu, H. Katsura, S.-W. Li, X. Cai, and X.-W. Guan, Exact solutions of few-magnon problems in the spin-S periodic XXZ chain, Phys. Rev. B **105**, 064419 (2022).
[118] M. Takahashi, *Thermodynamics of One-Dimensional Solvable Models* (Cambridge University Press, Cambridge, UK, 1999).
[119] F. H. L. Essler, H. Frahm, F. Göhmann, A. Klümper, and V. E. Korepin, *The One-Dimensional Hubbard Model* (Cambridge University Press, Cambridge, UK, 2005).
[120] https://github.com/Q-WAVES/GiantAtoms/.
[121] X. Wang, J.-Q. Li, Z. Wang, A. F. Kockum, L. Du, T. Liu, and F. Nori, Nonlinear cascaded quantum network with giant emitters, Commun. Phys. **9**, 205 (2026).